A New Multivariate Statistical Model for Change Detection in Images Acquired by Homogeneous and Heterogeneous Sensors

Jorge Prendes, Marie Chabert, Frédéric Pascal, Alain Giros, Jean-Yves Tourneret

▶ To cite this version:

Jorge Prendes, Marie Chabert, Frédéric Pascal, Alain Giros, Jean-Yves Tourneret. A New Multivariate Statistical Model for Change Detection in Images Acquired by Homogeneous and Heterogeneous Sensors. IEEE Transactions on Image Processing, Institute of Electrical and Electronics Engineers, 2015, 24 (3), pp.799-812. <10.1109/TIP.2014.2387013>. <hal-01127988>

HAL Id: hal-01127988
https://hal.archives-ouvertes.fr/hal-01127988

Submitted on 9 Mar 2015

HAL is a multi-disciplinary open access archive for the deposit and dissemination of scientific research documents, whether they are published or not. The documents may come from teaching and research institutions in France or abroad, or from public or private research centers.

L'archive ouverte pluridisciplinaire **HAL**, est destinée au dépôt et à la diffusion de documents scientifiques de niveau recherche, publiés ou non, émanant des établissements d'enseignement et de recherche français ou étrangers, des laboratoires publics ou privés.

Open Archive Toulouse Archive Ouverte (OATAO)
OATAO is an open access repository that collects the work of Toulouse researchers and makes it freely available over the web where possible.

This is an author-deposited version published in: http://oatao.univ-toulouse.fr/
Eprints ID: 13621

Identification number: DOI: 10.1109/TIP.2014.2387013
Official URL: http://dx.doi.org/10.1109/TIP.2014.2387013

To cite this version:
Prendes, Jorge and Chabert, Marie and Pascal, Frédéric and Giros, Alain and Tourneret, Jean-Yves *A New Multivariate Statistical Model for Change Detection in Images Acquired by Homogeneous and Heterogeneous Sensors*. (2015) IEEE Transactions on Image Processing, vol. 24 (n° 3). pp. 799-812. ISSN 1057-7149

Any correspondence concerning this service should be sent to the repository administrator: staff-oatao@inp-toulouse.fr

A New Multivariate Statistical Model for Change Detection in Images Acquired by Homogeneous and Heterogeneous Sensors

Jorge Prendes, *Student Member, IEEE*, Marie Chabert, *Member, IEEE*, Frédéric Pascal, *Senior Member, IEEE*,
Alain Giros, and Jean-Yves Tourneret, *Senior Member, IEEE*

***Abstract*— Remote sensing images are commonly used to monitor the earth surface evolution. This surveillance can be conducted by detecting changes between images acquired at different times and possibly by different kinds of sensors. A representative case is when an optical image of a given area is available and a new image is acquired in an emergency situation (resulting from a natural disaster for instance) by a radar satellite. In such a case, images with heterogeneous properties have to be compared for change detection. This paper proposes a new approach for similarity measurement between images acquired by heterogeneous sensors. The approach exploits the considered sensor physical properties and specially the associated measurement noise models and local joint distributions. These properties are inferred through manifold learning. The resulting similarity measure has been successfully applied to detect changes between many kinds of images, including pairs of optical images and pairs of optical-radar images.**

***Index Terms*— Optical images, SAR images, change detection, EM algorithm, mixture models, manifold learning.**

I. INTRODUCTION

FOR a long time, airborne or satellite remote sensing imagery has been used to track changes on the Earth surface for applications including urban growth tracking [1], [2], plantation monitoring, and urban database updating [3]. For this purpose, different sensors have been investigated including optical [4], synthetic aperture radars (SAR) [4]–[6] or multi-spectral sensors [4]. Due to the involved wavelengths, optical sensors provide high resolution images. As a consequence, huge databases of optical images are currently available. On the other hand, SAR images can be acquired even at night or under bad weather conditions and thus are more rapidly available in emergency situations [7]. Consequently, accurate change detectors applying to either homogeneous or heterogeneous sensors are needed for the management of natural disasters such as floods, volcano eruptions or earthquakes [8].

Change detection is the discrimination of two different classes representing change and no change between two images. In this paper we focus on the analysis of multitemporal coregistered remote sensing images. The features handled by change detection methods are generally chosen according to the kind of sensor. As a consequence many different approaches have been developed for optical and SAR images separately. In this paper we propose a new flexible change detection strategy capable of dealing with homogeneous and heterogeneous sensors (with a specific attention to detecting changes between optical and SAR images).

In the case of optical images, many detection methods are based on the difference between intensities or on the difference between spectral bands in the case of multispectral images leading to the so-called spectral change vector [9]. The difference image was initially derived pixel-wise [10]–[14]. However a parcel-wise derivation, using local averaging increases robustness with respect to noise, misregistration, miscalibration and other artifacts [15], [16]. Note that the difference image can also be derived in a transformed domain related to the wavelet transform for instance [17], [18]. Some interesting change detection methods adapted to optical images are based on neural networks [19]–[22] and support vector machines [23], [24]. Finally, it is interesting to mention that a survey of many popular change detection methods was made in [25].

In the case of SAR images, many change detection methods are based on the ratio of the image intensities because of the multiplicative nature of the sensor noise [26]–[31]. In this case the difference image is usually computed as the difference between the logarithm of the images, which is referred as the log-ratio. As in the case of optical images, some change detection methods are based on neural networks [32], [33] or on the joint distribution of the two images [34]–[36].

This work was partially supported by the ANR11LABX0040CIMI during the program ANR-11-IDEX-0002-02 within the thematic trimester on image processing.

J. Prendes is with the TéSA Laboratory, Toulouse 31500, France (e-mail: jorge.prendes@tesa.prd.fr).

M. Chabert and J.-Y. Tourneret are with the INP/École Nationale Supérieure d'Électronique, d'Électrotechnique, d'Informatique, d'Hydraulique et des Télécommunications-Institut de Recherche en Informatique de Toulouse, University of Toulouse, Toulouse 31062, France (e-mail: marie.chabert@enseeiht.fr; jean-yves.tourneret@enseeiht.fr).

F. Pascal is with Supélec, Gif-sur-Yvette 91190, France (e-mail: frederic.pascal@supelec.fr).

A. Giros is with the Centre National d' Études Spatiales, Toulouse 31400, France (e-mail: alain.giros@cnes.fr).

Digital Object Identifier 10.1109/TIP.2014.2387013

The correlation coefficient is particularly popular for detecting changes between images acquired by homogeneous sensors [37]. In this case, it is assumed that, in the absence of change, the pixel intensities in the two images are linearly correlated. However, this assumption is generally not valid in the case of heterogeneous sensors [7], [37]–[39]. The mutual information allows the dependency between two non linearly dependent images to be measured. The estimation of the mutual information requires estimating the joint distribution of the pixel intensities, which can be achieved using a joint histogram or methods based on Parzen windows [40]. Unfortunately, the resulting mutual information is strongly dependent on the bins used to generate the histogram [41] or on the Parzen window size [40]. More robust techniques are required to estimate the joint distribution of the images of interest and their mutual information. One alternative is to consider parametric distributions and to estimate their parameters using pixels located within a sliding window. Distributions that have been recently considered in the literature include bivariate gamma distributions for two SAR images [34]. Extensions to heterogeneous sensors, where the statistics of the two marginal distributions are not necessarily the same have also been proposed in [37] and [42].

However, change detection between images acquired by heterogeneous sensors has received much less attention in the literature than the optical/optical or radar/radar cases. One can cite the recent approach developed in [43] which transforms one of the two images in order to obtain characteristics similar to the other image, using the theory of copulas. However, this method requires to learn the appropriate copula using training samples and it is hardly generalizable to situations where more than two images are available.

This paper proposes a new method to estimate the joint distribution of pixel intensities based on a physical model. We assume that we have observed a given scene through a set of D images denoted as $\{I_1, \dots, I_D\}$ acquired by D sensors $\{S_1, \dots, S_D\}$. Each sensor has imaged the scene differently, e.g., a given sensor measures different physical properties of the objects involved in the scene and the kind of noise affecting these measures generally differs from one sensor to another. Consider as an example the case of two optical and SAR images ($D = 2$). The SAR sensors are very sensitive to the object edges whereas the colorimetry of a scene is clearly an important property captured by optical sensors. The noise affecting a given area of a homogeneous SAR image is classically supposed to be a multiplicative speckle noise with gamma or Weibull distribution [44]–[46]. Conversely, the noise affecting optical images has been considered as an additive Gaussian noise in many applications [47], [48]. The model considered in this study takes advantage of the relationships between the sensor responses to the objects contained in the observed scene, the physical properties of these objects and the statistical properties of the noise corrupting the images. The proposed model is flexible in the sense that it can be used for images acquired with homogeneous (e.g., two optical or two SAR) or heterogeneous sensors (e.g., one optical and one SAR) and for many kinds of sensors simultaneously. The parameters of this model can be estimated by the popular expectation-maximization (EM) algorithm [49], [50]. A similarity measure between sliding windows contained in the observed images is then derived from this model. This similarity measure is potentially interesting for many image processing applications. Our paper focuses on its application to detect changes between optical and SAR images. However the proposed statistical model can be applied to any kind of images acquired in single or multiple channels. Moreover, the similarity measure associated with this model can be interesting for many other applications including image registration and image indexing.

The paper is structured as follows. Section II introduces the new statistical model used to describe the pixel intensity distribution of a set of images acquired with either homogeneous or heterogeneous sensors. A method for generating synthetic images based on such model is also presented. Section III begins with a description of classical similarity measures and an analysis of their weaknesses. A new flexible similarity measure based on the model investigated in the previous section is finally defined. Change detection results obtained with this similarity measure for various synthetic and real images are presented in Section IV. Conclusions, possible improvements and future work are reported in Section V.

II. A NEW STATISTICAL MODEL FOR IMAGE ANALYSIS

This section introduces a flexible statistical model for the pixel intensities associated with several images acquired by different sensors. To achieve this, the marginal statistical properties of the pixel intensities contained in a homogeneous area are reviewed in Section II-A. Section II-B defines the joint distribution of a group of pixels belonging to a homogeneous area contained into the analysis window. An extension to pixels belonging to a non-homogeneous area is introduced in Section II-C.

A. Statistical Properties of Homogeneous Areas

A homogeneous area of an image is a region of the image where the pixels have the same physical properties (denoted as P). Since the measurements of any sensor S are corrupted by noise, we propose the following statistical model for the image intensity I_S associated with the sensor S

$$I_S | P = f_S[T_S(P), \nu_S] \tag{1}$$

where

- P is used for the set of physical properties characterizing the homogeneous area
- $T_S(P)$ is a deterministic function of P explaining how an ideal noiseless sensor S would capture these physical properties P to form an intensity
- ν_S is a random variable representing the sensor noise (which only depends on S).
- $f_S(\cdot, \cdot)$ describes how the sensor noise interacts with the ideal sensor measurement (which only depends on the kind of sensor S)

Model (1) indicates that I_S is a random variable whose distribution depends on the noise distribution but also on $T_S(P)$.

In order to clarify this point, the examples of SAR and optical images are considered in what follows.

For SAR images, it is widely accepted that the pixel intensity I_{SAR} in a homogeneous area is distributed according to a gamma distribution [44]–[46], and that the so-called speckle noise is multiplicative. Thus, for this example the model (1) reduces to

$$I_{\mathrm{SAR}}|P = T_{\mathrm{SAR}}(P)\, \nu_{\mathrm{SAR}}$$

where T_{SAR} is the functional transforming the physical properties of the scene P to the noiseless radar intensity and ν_{SAR} is a multiplicative speckle noise with gamma distribution, i.e., $\nu_{\mathrm{SAR}} \sim \Gamma\left(L, L^{-1}\right)$, where L is the so-called number of looks of the SAR sensor. Using standard results on gamma distributions, we obtain

$$I_{\mathrm{SAR}}|P \sim \Gamma\left[L, \frac{T_{\mathrm{SAR}}(P)}{L}\right]. \tag{2}$$

For optical images, we can consider that the pixel intensity I_{Opt} is affected by an additive Gaussian noise [47] leading to

$$I_{\mathrm{Opt}}\big|P = T_{\mathrm{Opt}}(P) + \nu_{\mathrm{Opt}}$$

where T_{Opt} is the optical equivalent of T_{SAR} (i.e., the functional indicating the true color of the object with physical properties P) and the random variable ν_{Opt} is an additive Gaussian noise with constant variance σ^2, i.e., $\nu_{\mathrm{Opt}} \sim \mathcal{N}\left(0, \sigma^2\right)$. These assumptions lead to

$$I_{\mathrm{Opt}}\big|P \sim \mathcal{N}\left[T_{\mathrm{Opt}}(P), \sigma^2\right]. \tag{3}$$

Taking the optical grayscale sensor as an example, we have

$$T_{\mathrm{Opt}}(P) = \frac{R+G+B}{3} \tag{4}$$

where R, G and B are the red, green and blue components respectively of the noiseless color image, which can be easily derived from the material reflectivity (contained in P) and the spectral response of each color filter in the sensor.

The notations $\Gamma_P(I_{\mathrm{SAR}})$ and $\mathcal{N}_P\left(I_{\mathrm{Opt}}\right)$ will be used in this paper to denote the probability density functions (pdfs) of $I_{\mathrm{SAR}}|P$ and $I_{\mathrm{Opt}}\big|P$.

B. Distribution for Multiple Sensors in a Homogeneous Area

Assume that we have observed D images acquired by D different and independent sensors. It makes sense to assume that the D random variables $\nu_1, \ldots, \nu_D$ (defining the random vector $\boldsymbol{\nu} = (\nu_1, \ldots, \nu_D)^T$) associated with the sensor noises are independent. Since the image intensity $I_d|P$ only depends on ν_d for any $d = 1, \ldots, D$, the joint distribution of the image intensities is

$$p(I_1, \ldots, I_D|P) = \prod_{d=1}^{D} p(I_d|P). \tag{5}$$

For example, in the (interesting) particular case where one radar and one optical image are observed, one obtains

$$p\left(I_{\mathrm{SAR}}, I_{\mathrm{Opt}}\big|P\right) = \Gamma_P(I_{\mathrm{SAR}})\, \mathcal{N}_P\left(I_{\mathrm{Opt}}\right).$$

C. Distribution for Multiple Sensors in a Sliding Window

A classical way of handling the change detection problem for a set of D images is to analyze these images using sliding windows and to define a change indicator for each window [38]. In this case, we are particularly interested in the statistical properties of the pixel intensities within a sliding window. Denote as $p(I_1, \ldots, I_D|W)$ the joint pdf of the pixel intensities within a sliding window W. To obtain this pdf, we assume that the region of interest (located inside the sliding window) is composed of a finite number K of homogeneous areas with different physical properties $P_1, \ldots, P_K$. In this case, it makes sense to assume that the physical properties of the region of interest can be described by a discrete random variable with distribution

$$p(P|W) = \sum_{k=1}^{K} w_k\, \delta(P - P_k) \tag{6}$$

where w_k is the weight or probability of P_k which represents the relative area of W covered by P_k. Using (5) and the total probability theorem, the joint distribution of the pixel intensity can be expressed as

$$\begin{aligned} p(I_1, \ldots, I_D|W) &= \sum_{k=1}^{K} w_k\, p(I_1, \ldots, I_D|P_k) \\ &= \sum_{k=1}^{K} w_k \prod_{d=1}^{D} p(I_d|P_k). \end{aligned} \tag{7}$$

In the particular case of two SAR and optical images, we obtain

$$p\left(I_{\mathrm{SAR}}, I_{\mathrm{Opt}}\big|W\right) = \sum_{k=1}^{K} w_k\, \Gamma_{P_k}(I_{\mathrm{SAR}}) \mathcal{N}_{P_k}\left(I_{\mathrm{Opt}}\right). \tag{8}$$

The expressions (7) and (8) show that the joint distribution of the pixel intensities within a given sliding window W is a mixture of distributions. Moreover, according to (5), each component of this mixture is the product of densities associated with independent random variables. Some remarks are appropriate here:

Remark 1: In the case of multispectral images, each spectral band can be considered as a separate image. If we assume that the noises affecting each band are independent Gaussian random variables, equations (3) and (5) are satisfied. In this case, the noise vector associated with the multispectral image is distributed according to a multivariate normal distribution with a diagonal covariance matrix.

Remark 2: The way we have decomposed the observed images into sliding windows deserves some comment. First, the change detection strategy considered in this paper relies on the properties of sliding windows containing different objects. The proposed similarity measure and the corresponding change detection rule are related to the entire sliding window and not to a specific pixel of this window (such as its centroid for instance). Thus, considering too many overlapping windows (e.g., with many common pixels) is not useful. Indeed, when two windows are very similar, the estimated pdf are mostly the same (with some slight

(a) Rural I_{SAR} (b) Rural I_{Opt} (c) Urban I_{Opt}

Fig. 1. Examples of real SAR (a) and optical (b) images for a rural area (near Gloucester, UK), and of an optical (c) image for an urban area (in south Toulouse, FR).

changes in the weights, or with the creation/removal of small weighted mixture components) which reduces diversity. Moreover, the computational complexity of the change detection is directly related to the number of windows associated with the images to be analyzed. In our implementations, we have analyzed the images of interest using sliding windows of size $N = p \times p$ with p even and 50% overlap between two consecutive windows, so that the window (i, j) corresponds to the pixels $\left[\frac{p}{2}(i-1)+1, \frac{p}{2}(i+1)\right] \times \left[\frac{p}{2}(j-1)+1, \frac{p}{2}(j+1)\right]$ on the image. Within a given window, some objects can change when the others do not change. Each pixel in the sliding window has a pdf defined by (7) and all the pixels belonging to a given window are statistically independent conditionally to the set of properties $P_1, \ldots, P_K$.

D. Synthetic Images

This section summarizes the different steps that have been considered to generate synthetic images for understanding and evaluating the performance of the proposed change detection algorithms. From the model introduced in (1), a synthetic image can be generated from the knowledge of

- The distribution of the noise ν_S,
- The transformation $T_S(\cdot)$,
- The function $f_S(\cdot,\cdot)$,
- An image representing the values of P.

For most sensors (particularly for optical and SAR sensors), the distribution of ν_S as well as the function $f_S(\cdot,\cdot)$ are known, while the transformation $T_S(P)$ is unknown and depends on the chosen representation of P. In this paper, we propose to generate a synthetic image P and to transform it using a known transformation $T_S(P)$. Looking at real images such as those depicted in Fig. 1, we can see that they are composed of different patches with homogeneous properties. Considering this, we have generated a synthetic image P by defining different regions in the image and have assigned them a random value of P. To define the different regions, random points are distributed within a rectangular area. These points will represent the nodes of the polygons delimiting each region. The edges of these polygons are obtained through a Delaunay triangulation [51]. The prior distribution of P within each polygon being unknown, we have drawn the values of P according to a uniform distribution in the set [0, 1]. A typical example of image obtained with this approach is depicted in Fig. 2(a).

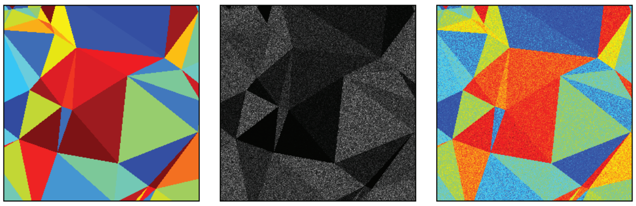

(a) (b) (c)

Fig. 2. Synthetic P image and its corresponding SAR and optical images. (a) P Image. (b) I_{SAR}. (c) I_{Opt}.

The second point required for the generation of synthetic images is the definition of the transformation T_S for each sensor. For instance, consider grayscale optical and SAR sensors. For the optical sensor, $T_{\mathrm{Opt}}(P)$ can be defined as $T_{\mathrm{Opt}}(P) = \frac{R+G+B}{3}$ as in (4). In order to test our algorithm, we have defined a SAR response $T_{\mathrm{SAR}}(\cdot)$ which is not linearly correlated with $T_{\mathrm{Opt}}(\cdot)$ given by

$$T_{\mathrm{SAR}}(P) = T_{\mathrm{Opt}}(P)\left[1 - T_{\mathrm{Opt}}(P)\right]. \tag{9}$$

The final images are obtained by corrupting $T_{\mathrm{Opt}}(P)$ and $T_{\mathrm{SAR}}(P)$ by additive and multiplicative noise as in (2) and (3). Examples of images simulated with this method are displayed in Figs. 2(b) and 2(c). To generate synthetic changes corresponding to different areas of the images, different values of P have been chosen for the two sensors. This strategy can also be used to generate images with some regions affected by changes and some other regions not affected by any change.

E. Model Parameter Estimation

Different approaches have been widely used in the literature to estimate the parameters of a mixture distribution such as (7) or (8). Even if the method of moments has received some interest for this estimation problem [52], the EM algorithm has became a reference for mixture models [53], [54]. The EM algorithm is known to converge to a local maximum of the likelihood function [49]. When applied to the joint distribution (7), the algorithm iteratively optimizes the following Q function defined as an expectation (E-step)

$$Q\left(\boldsymbol{\theta}\middle|\boldsymbol{\theta}^{(i)}\right) = \mathrm{E}_{\boldsymbol{K}\left|\boldsymbol{I},\boldsymbol{\theta}^{(i)}\right.}\left[\log p(\boldsymbol{I},\boldsymbol{K}|\boldsymbol{\theta})\right] \tag{10}$$

where

- $\boldsymbol{I} = [\boldsymbol{I}_1, \ldots, \boldsymbol{I}_N]$ represents the observed data, N is the number of pixels in the window W, and $\boldsymbol{I}_n = \left[I_{S_1}, \ldots, I_{S_D}\right]_n$ (with $n = 1, \ldots, N$) contains the intensities for the n-th pixel produced by the different sensors,
- $\boldsymbol{\theta} = [\boldsymbol{\theta}_1, \ldots, \boldsymbol{\theta}_K]$ is the set of parameters defining the mixture, where $\boldsymbol{\theta}_k = \left[w_k, \boldsymbol{\theta}_{k,1}, \ldots, \boldsymbol{\theta}_{k,D}\right]$ with $k = 1, \ldots, K$ contains the parameters related to the k-th object (or equivalently, the k-th mixture component)
  - w_k is the proportion of P_k in the window W,
  - $\boldsymbol{\theta}_{k,d}$ is the set of parameters for the sensor S_d that defines the distribution resulting from the physics of the component P_k,
- $\boldsymbol{\theta}^{(i)}$ is the value of the parameter $\boldsymbol{\theta}$ on the i-th iteration of the algorithm,

- $\boldsymbol{K} = [k_1, \ldots, k_N]$ is the unobserved map of labels indicating that pixel $\boldsymbol{I}_n$ results from the observation of the k-th component P_k.

At each iteration the optimization (M-step) is performed

$$\boldsymbol{\theta}^{(i+1)} = \arg\max_{\boldsymbol{\theta}} Q\left(\boldsymbol{\theta}\middle|\boldsymbol{\theta}^{(i)}\right).$$

It can be easily proven that optimizing $Q\left(\boldsymbol{\theta}\middle|\boldsymbol{\theta}^{(i)}\right)$ with respect to (wrt) $\boldsymbol{\theta}$ is equivalent to optimizing $\log p(\boldsymbol{I}|\boldsymbol{\theta})$ wrt $\boldsymbol{\theta}$ [53].

Throughout this paper, we consider the standard assumption according to which the samples $[\boldsymbol{I}_1, k_1], \ldots, [\boldsymbol{I}_N, k_N]$ are independent (independence of the pixels in the observation window) leading to

$$\log p(\boldsymbol{I}, \boldsymbol{K}|\boldsymbol{\theta}) = \sum_{n=1}^{N} \log p(\boldsymbol{I}_n, k_n|\boldsymbol{\theta}).$$

Thus, using the linearity of the expectation, (10) can be rewritten as

$$\begin{aligned} Q\left(\boldsymbol{\theta}\middle|\boldsymbol{\theta}^{(i)}\right) &= \mathrm{E}_{\boldsymbol{K}|\boldsymbol{I},\boldsymbol{\theta}^{(i)}}\left[\sum_{n=1}^{N} \log p(\boldsymbol{I}_n, k_n|\boldsymbol{\theta})\right] \\ &= \sum_{n=1}^{N} \mathrm{E}_{k_n|\boldsymbol{I}_n,\boldsymbol{\theta}^{(i)}}\left[\log p(\boldsymbol{I}_n, k_n|\boldsymbol{\theta})\right]. \end{aligned} \qquad (11)$$

Since k_n is a discrete variable, its expected value can be written as a summation, i.e., for any function $g(\cdot)$, we have

$$\begin{aligned} \mathrm{E}_{k_n|\boldsymbol{I}_n,\boldsymbol{\theta}^{(i)}}[g(k_n)] &= \sum_{k=1}^{K} p\left(k_n = k\middle|\boldsymbol{I}_n, \boldsymbol{\theta}^{(i)}\right) g(k_n = k) \\ &= \sum_{k=1}^{K} \frac{p\left(\boldsymbol{I}_n, k_n = k\middle|\boldsymbol{\theta}^{(i)}\right)}{p\left(\boldsymbol{I}_n\middle|\boldsymbol{\theta}^{(i)}\right)} g(k_n = k) \\ &= \sum_{k=1}^{K} \pi_{n,k}^{(i)} f(k_n = k) \end{aligned} \qquad (12)$$

where $\pi_{n,k}^{(i)} = \frac{p\left(\boldsymbol{I}_n, k_n=k\middle|\boldsymbol{\theta}^{(i)}\right)}{p\left(\boldsymbol{I}_n\middle|\boldsymbol{\theta}^{(i)}\right)}$ is constant for a given value of (i, n, k).

Replacing (12) in (11), Q can be expressed as

$$\begin{aligned} Q\left(\boldsymbol{\theta}\middle|\boldsymbol{\theta}^{(i)}\right) &= \sum_{n=1}^{N}\sum_{k=1}^{K} \pi_{n,k}^{(i)} \log p(\boldsymbol{I}_n, k_n = k|\boldsymbol{\theta}) \\ &= \sum_{n=1}^{N}\sum_{k=1}^{K} \pi_{n,k}^{(i)} \log\left[w_k\, p(\boldsymbol{I}_n|k_n = k, \boldsymbol{\theta})\right] \\ &= \sum_{n=1}^{N}\sum_{k=1}^{K} \pi_{n,k}^{(i)} \log w_k \\ &\quad + \sum_{n=1}^{N}\sum_{k=1}^{K} \pi_{n,k}^{(i)} \log p(\boldsymbol{I}_n|\boldsymbol{\theta}_k). \end{aligned}$$

It should be noted that $p(\boldsymbol{I}_n|\boldsymbol{\theta}_k) = p(\boldsymbol{I}_n|k_n = k, \boldsymbol{\theta})$ is the probability that the observed pixel intensities $\boldsymbol{I}_n$ are produced by an object with physical properties P_k. Thus, $p(\boldsymbol{I}_n|\boldsymbol{\theta}_k)$ can be replaced by the result obtained in (5) leading to


(a) (b) (c)

Fig. 3. Images of an unchanged area in south of Toulouse and the corresponding joint distribution. (a) I_{old}. (b) I_{new}. (c) $p(I_{\text{old}}, I_{\text{new}})$.

$$\begin{aligned} Q\left(\boldsymbol{\theta}\middle|\boldsymbol{\theta}^{(i)}\right) &= \sum_{n=1}^{N}\sum_{k=1}^{K} \pi_{n,k}^{(i)} \log w_k \\ &\quad + \sum_{n=1}^{N}\sum_{k=1}^{K}\sum_{d=1}^{D} \pi_{n,k}^{(i)} \log p\left(I_{n,d}\middle|\boldsymbol{\theta}_{k,d}\right). \end{aligned} \qquad (13)$$

This result shows that Q can be written as the summation of negative terms, where each term depends on the different components $\boldsymbol{\theta}_{k,d}$ of $\boldsymbol{\theta}$. This implies that each term can be maximized independently w.r.t. $\boldsymbol{\theta}_{k,d}$. Moreover, maximizing Q w.r.t. w_k yields

$$w_k^{(i+1)} = \frac{1}{N}\sum_{n=1}^{N} \pi_{n,k}^{(i)}$$

while maximizing Q w.r.t. $\boldsymbol{\theta}_{k,d}$ leads to

$$\boldsymbol{\theta}_{k,d}^{(i+1)} = \arg\max_{\boldsymbol{\theta}_{k,d}} \sum_{n=1}^{N} \pi_{n,k}^{(i)} \log p\left(I_{n,d}\middle|\boldsymbol{\theta}_{k,d}\right) \qquad (14)$$

which is the weighted maximum likelihood estimator (MLE) of the pdfs associated with the sensors S_d for $d = 1, \ldots, D$. Note that the optimization problem (14) has been solved for most well known distributions [55]. Note also that estimating the parameters of the proposed model for a given set of heterogeneous sensors reduces to determining the parameter MLEs for each sensor independently. However, the number of components in the mixture should also be estimated, which should correspond to the number of objects present in the window W. The algorithm introduced in [56] can be used for this estimation. This algorithm starts with an upper bound of the number of components, and gradually removes the components that do not describe enough samples.

III. SIMILARITY MEASURES

A. Analysis of Classical Similarity Measures

This section uses the statistical model introduced in Section II-C to analyze the behavior of the correlation coefficient and the mutual information as change indicators. Figs. 3(a) and 3(b) display examples of optical images associated with an unchanged area. Three kinds of objects can be clearly seen in these two images: a red roof, grass, and parts of trees. According to the proposed model, the joint distribution of these images should be a mixture of three

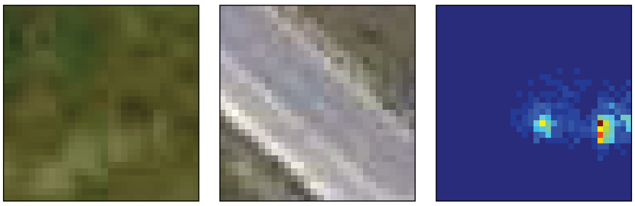

(a) (b) (c)

Fig. 4. Images before and after the construction of a road in south of Toulouse and the corresponding joint distribution. (a) I_{old}. (b) I_{new}. (c) $p(I_{\text{old}}, I_{\text{new}})$.

Gaussian components. Fig. 3(c) shows the estimated joint distribution of the two images. This distribution has been estimated using a histogram, which was computed using an appropriate number of bins obtained by cross validation. The centroids of the clusters contained in Fig. 3(c) are close to a straight line defined by $\mu_{S_1} = \lambda\, \mu_{S_2} + \beta$. The parameters λ and β account for contrast and brightness differences as explained in [57]. This result is easy to understand since the two images have been acquired by the same kind of sensor.

Figs. 4(a) and 4(b) show a pair of optical images corresponding to a changed area. The first image is quite homogeneous and is mainly composed of grass. A new road takes most of the central portion of the second image. The first image can be thought as having the same object distribution as the second one, where some of the objects have different physical properties P on each of the two images. Since two different objects are present in the second image, the joint distribution of the two images is expected to have two components, where the parameters of the first dimension are the same for both components (since this first dimension corresponds to the same object, i.e., the grass). This result can be clearly seen in Fig. 4(c). It should also be noted that since there is a changed area between the two images, the two components are aligned in a horizontal (or vertical) line (as for the unchanged area of 3). Note finally that the mutual information and the correlation coefficient are good similarity measures to detect changes corresponding to these situations.

However, the mutual information and the correlation coefficient are not always good similarity measures. For instance, these measures provide similar results when only one object is contained within the window (as would often happen when using small windows, or when using high resolution images), independently of the presence of a change or not. An example of this situation is illustrated in Figs. 5 and 6. Figure 5 shows two windows in the presence of a change, where the corresponding joint distribution (estimated using a 2D histogram with 50 $\times$ 50 bins in the normalized range $[0,1] \times [0,1]$) shows two independent variables. This independence may indicate a change between the thwo images. Fig. 6 shows two windows of an unchanged area in two different times, however its joint distribution (also estimated with 50×50 bins in the normalized range $[0,1] \times [0,1]$) also shows two independent variables, and thus, change detectors based on statistical independence would lead to a wrong result. Applying the model (7) to these situations, P will be constant in each window: in one situation both images will share the same value of P, and in the other situation the new value of P denoted as P_{new} will be different from the old value of P denoted as P_{old}. However, in both cases, the joint distribution consists of only one cluster. In these cases the mutual information, the correlation coefficient, or any dependency measure are clearly bad similarity measures.

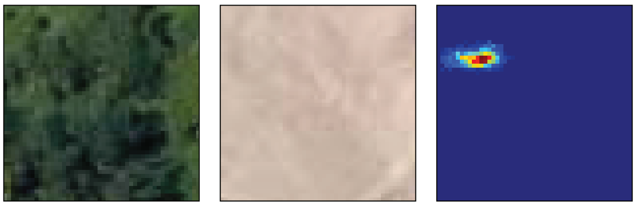

(a) (b) (c)

Fig. 5. Old image with a group of trees, new image preparing the ground for a new construction, and their corresponding joint distribution. (a) I_{old}. (b) I_{new}. (c) $p(I_{\text{old}}, I_{\text{new}})$.

(a) I_{old} (b) I_{new} (c) $p(I_{\text{old}}, I_{\text{new}})$

Fig. 6. (a) and (b) Optical images for an unchanged homogeneous area with different brightnesses and contrasts, and (c) the corresponding joint distribution (estimated using a 2D histogram).

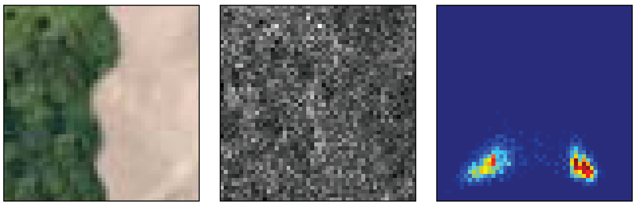

(a) I_{old} (b) I_{new} (c) $p(I_{\text{old}}, I_{\text{new}})$

Fig. 7. (a) Optical image with two different objects, (b) the unchanged image corresponding to a sensor with $T_S(P) = T_{\text{Opt}}(P)\big[1 - T_{\text{Opt}}(P)\big]$ and (c) the corresponding joint distribution (estimated using a 2D histogram).

Another situation where measures based on the dependency of two random variables fail to detect changes is presented in Fig. 7. This situation corresponds to an optical sensor defined by $T_{\text{Opt}}(P)$ and another sensor defined by $T_S(P) = T_{\text{Opt}}(P)\big[1 - T_{\text{Opt}}(P)\big]$. As it can be seen in Fig. 7(c), the values of the intensities for the left and right sides of the optical image are quite different (close to 0.25 and to 0.75 respectively). However, because of the transformation T_S, the transformed values $T_S(P)$ for the sensor S are both similar, making I_S homogeneous. The resulting joint distribution between the two images consists of two clusters aligned in a horizontal (or vertical) line, as shown in Fig. 7(c). In this situation, the correlation coefficient and the mutual information are not appropriate to detect the absence of change between the two images.

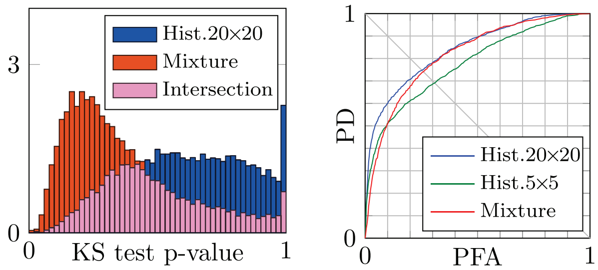

(a) KS test for two pdf estimators. (b) ROCs using mutual information.

Fig. 8. The improved goodness of fit obtained with the mixture pdf (a) does not reflect any improvement in the change detection performance (b) when compared to the use of the mutual information as a similarity measure.

Another factor to consider is that whenever we compute a similarity measure, we discard some information considered as irrelevant and we keep some information considered as relevant. These irrelevant and relevant quantities are summarized into a single quantity, namely the similarity measure. When considering the mutual information or the correlation coefficient, we arbitrarily decide that the relevant information is contained solely in the dependency of the two random variables. This property yields a limit on the performance that can be obtained using this similarity measure. Even when the joint distribution estimation is improved, the resulting change detection performance is not necessarily improved when using the mutual information as a similarity measure. To measure the estimation improvement, a 2D generalization of the Kolmogorov-Smirnov (KS) goodness of fit test [58] was used. This test measures whether a sample population has been produced by a given distribution or not. The hypothesis H_0 indicating that the sample population was produced by the same distribution is accepted whenever the p-value is less than the significance level α. Fig. 8(a) shows that when using a mixture to estimate the joint distribution, the resulting goodness of fit is improved with respect to that obtained with a histogram. However, the receiver operating characteristic (ROC) curves [59] in Fig. 8(b) show that the performance obtained when using the mutual information to detect changes is not necessarily improved, motivating the definition of a new similarity measure.

B. Manifold Estimation

We propose to define a vector $\boldsymbol{v}_P$ gathering all the transformations $T_{S_d}(P)$ for $d = 1, \ldots, D$, i.e.,

$$\boldsymbol{v}_P = \left[T_{S_1}(P), \ldots, T_{S_D}(P)\right] \tag{15}$$

which is a parametric function of P defining a manifold in $\mathbb{R}^m$, where m is the dimension of the vector $\boldsymbol{v}_P$. Note that m can be different from D since any sensor can provide several measurements, e.g., a typical optical camera produces 3 measurements for each pixel. The vector $\boldsymbol{v}_p$ defines a manifold characterizing the relationships between the sensors involved. For instance, for a color optical sensor S_1 such that $T_{S_1}(P) = [R, G, B]$, and another optical sensor S_2 differing only by its brightness and contrast such that $T_{S_2}(P) = \lambda_1 T_{S_1}(P) + \lambda_2$ [57], the vector $\boldsymbol{v}_P$ is defined as

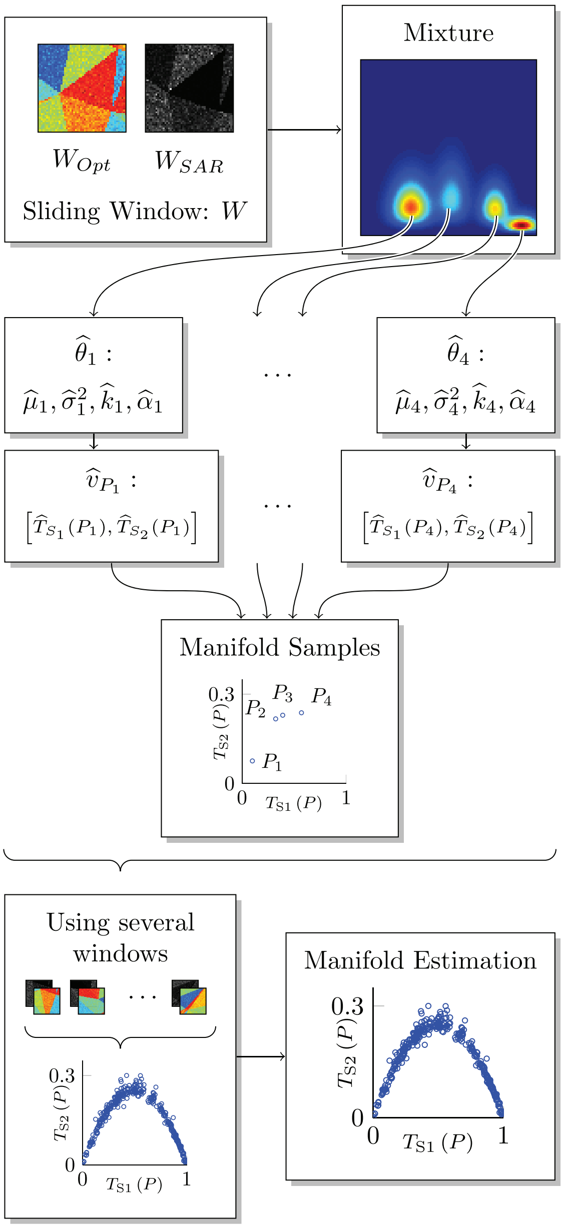

Fig. 9. Diagram illustrating the steps proposed for estimating the manifold described by $\boldsymbol{v}_P$ for a pair of synthetic images.

$$\begin{aligned}\boldsymbol{v}_P &= \left[T_{S_1}(P), T_{S_2}(P)\right]\\ &= [R, G, B, \lambda_1 R + \lambda_2, \lambda_1 G + \lambda_2, \lambda_1 B + \lambda_2].\end{aligned}$$

Note that a more complex vector $\boldsymbol{v}_P$ could be defined if we consider other factors such as sensor saturations. This section studies a method to estimate such manifold defined by $\boldsymbol{v}_P$.

Since the transformations T_{S_d} for $d = 1, \ldots, D$ are *a priori* unknown, the proposed method estimates the manifold defined by $\boldsymbol{v}_P$ from training data, considering P as a hidden variable. The general idea is to divide the training area in different windows, to estimate $\boldsymbol{v}_P$ for any window (each window corresponds to several values of P) and finally, to estimate the manifold described by $\boldsymbol{v}_P$ based on these estimates. This estimation procedure illustrated in Figure 9 is detailed more precisely in what follows.

For any sliding window W, we can estimate the parameters of the joint distribution (7) using the method described in Section II-E. This estimation produces a vector $\widehat{\boldsymbol{\theta}}$ for each component of the mixture model (7). For instance, for a grayscale optical image and a SAR image, $\widehat{\boldsymbol{\theta}} = \left[\widehat{\mu}, \widehat{\sigma}, \widehat{k}, \widehat{\alpha}\right]$ where $\widehat{\mu}$ and $\widehat{\sigma}$ are the mean and variance of the normal distribution associated with the optical sensor as in (3), and $\widehat{k}$ and $\widehat{\alpha}$ are the shape and scale parameters of the gamma distribution associated with the SAR sensor as described in (2). As explained by (1), the parameters contained in $\boldsymbol{\theta}$ are tightly related to $T_S(P)$, so that $T_S(P)$ can be estimated from $\widehat{\boldsymbol{\theta}}$. For instance, consider the case of two optical and SAR images. Using (2) and (3), we obtain $\widehat{T}_{\text{SAR}}(P) = \widehat{k\alpha}$ and $\widehat{T}_{\text{Opt}}(P) = \widehat{\mu}$. From the parameter vector $\widehat{\boldsymbol{\theta}}_k$ associated with the k-th component of the mixture distribution, we obtain an estimation $\widehat{\boldsymbol{v}}_P = \left[\widehat{T}_{\text{Opt}}(P), \widehat{T}_{\text{SAR}}(P)\right]$ of a point belonging to the manifold. In the particular case of a pair of optical and SAR images, the parameter vector is $\boldsymbol{\theta} = [\mu, \sigma, k, \alpha]$. From (2) and (3) we have $T_{\text{Opt}} = \mu$ and $T_{\text{SAR}} = k\alpha$. Thus, the manifold is defined by $\boldsymbol{v} = [\mu, k\alpha]$ so that we can estimate it as $\widehat{\boldsymbol{v}} = \left[\widehat{\mu}, \widehat{k\alpha}\right]$. As illustrated in Fig. 9, repeating this process for several windows provides samples that can be used to estimate the manifold associated with $\boldsymbol{v}_P$.

The following remark is appropriate: the weight w_k is related to the number of pixels associated with the kth component of the mixture. Thus, the estimations $\widehat{\boldsymbol{v}}_P$ resulting from components with low weights have a higher variance and thus impact negatively the manifold estimation. To prevent this, we estimated the manifold from the samples $\widehat{\boldsymbol{v}}(P_k)$ associated with the weights w_k above the 90th percentile. The difference between the manifold estimates obtained using all vectors $\widehat{\boldsymbol{v}}_{P_k}$ and the vectors associated with the largest weights can be observed in Figs. 10(a) and 10(c). Discarding the estimations $\widehat{\boldsymbol{v}}_P$ corresponding to the smallest weights introduces some robustness in the manifold estimation hence a better estimation performance.

C. A New Similarity Measure for Change Detection

In this paper, we want to define a similarity measure between different (possibly heterogeneous) images for change detection. This similarity measure is defined using an estimator of the probability density function (pdf) of $\widehat{\boldsymbol{v}}_P$. This pdf can be estimated by several methods based on multidimensional histograms, Parzen windows, or mixture distributions. In this paper we have approximated the pdf of $\widehat{\boldsymbol{v}}_P$ by a mixture of multivariate normal pdfs constructed by the samples $\widehat{\boldsymbol{v}}_P$ yielding $\widehat{p}(\widehat{\boldsymbol{v}}_P)$. Fig. 10 shows typical examples of estimations obtained for synthetic images corresponding to

$$\boldsymbol{v}_P = \left[T_{\text{Opt}}(P), T_{\text{SAR}}(P)\right] \tag{16}$$

with $T_{\text{SAR}}(P) = T_{\text{Opt}}(P)\left[1 - T_{\text{Opt}}(P)\right]$. The approximated mixtures (black curves) are clearly in good agreement with the actual pdfs (red curves).

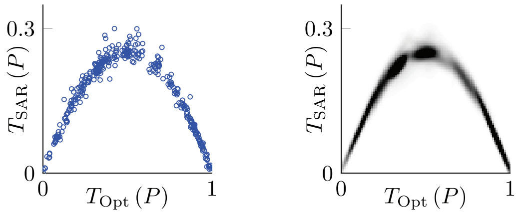

(a) $\boldsymbol{v}_P$ (red), $\widehat{\boldsymbol{v}}_{P_k}$ (blue). (b) $\boldsymbol{v}_P$ (red), $\widehat{p}(\widehat{\boldsymbol{v}}_P)$ (black).

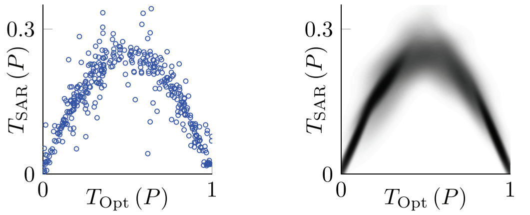

(c) $\boldsymbol{v}_P$ (red), $\widehat{\boldsymbol{v}}_{P_k}$ (blue). (d) $\boldsymbol{v}_P$ (red), $\widehat{p}(\widehat{\boldsymbol{v}}_P)$ (black).

Fig. 10. Manifold estimation for synthetic images obtained with the method described in Section III-B. Scatter plot of $\widehat{\boldsymbol{v}}_{P_k}$ for (a) high values of w_k and (c) any value of w_k, and their respective estimation of the pdf $\widehat{p}_T(\widehat{\boldsymbol{v}}_P)$.

D. New Change Detection Strategy

In order to build a new change detection strategy, we assume that two training images associated with an unchanged area are available. These images are used to estimate vectors $\widehat{\boldsymbol{v}}_P$ associated with the "no change" manifold. The corresponding pdf $\widehat{p}_T(\widehat{\boldsymbol{v}}_P)$ (where T stands for "Training") can then be estimated using the procedure presented in the previous section. We assume that the absence of change for the two kinds of images (for instance, an optical image and a SAR image) is characterized by the distribution of the vectors $\boldsymbol{v}_P$.

The change detection problem classically consists of detecting the absence and presence of changes into two test images. We propose to divide the two images into square estimation windows of size $p \times p$ [34], [38]. For any estimation window W containing p^2 pixels, we consider the following binary hypothesis testing problem

$$\begin{aligned} H_0 &: \text{Absence of change} \\ H_1 &: \text{Presence of change} \end{aligned}$$

A vector $\boldsymbol{v}_{W,k}$ (for $k = 1, \ldots, K$) is introduced to characterize the manifold associated with the k-th object within the estimation window W of the two test images. The procedure described in the previous section can then be used to estimate $\boldsymbol{v}_{W,k}$, obtaining as many vectors as components in the mixture distribution. Fig. 11 shows examples of estimates obtained with different test windows in the case of synthetic optical and SAR images, in the absence (Fig. 11(a)) and presence (Fig. 11(b)) of changes. Note that the synthetic images were generated with the method described in Section II-D, using the same P image for the "no change" test images, and using different P images for the "change" images. We can observe that the distances between the estimates $\widehat{\boldsymbol{v}}_{W,k}$ and $\boldsymbol{v}_P$ are clearly smaller for the windows associated with the "no change" test images, as expected. Based on these observations, we introduce the following similarity measure for a sliding

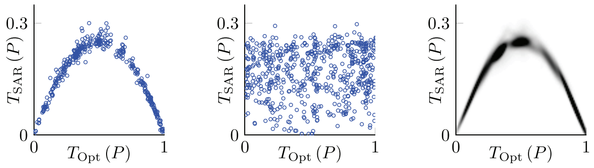

(a) Unchanged areas. (b) Changed areas. (c) $\widehat{p}_T(\widehat{\boldsymbol{v}}_P)$.

Fig. 11. Scatter plots of $\widehat{\boldsymbol{v}}_{W,k}$ (blue circles) for different areas of the images superimposed with the ideal $\boldsymbol{v}_P$ (red curve) (a) and (b). Corresponding estimated pdf $\widehat{p}_T(\widehat{\boldsymbol{v}}_P)$ (black) (c).

window W

$$\delta_W = \sum_{k=1}^{K} \widehat{\omega}_k \, \widehat{p}_T\left(\widehat{\boldsymbol{v}}_{W,k}\right) \tag{17}$$

where $\widehat{\omega}_k$ is the weight associated with the k-th object within W. This definition leads to the following change detection strategy

$$\log\left(\delta_W\right) \underset{H_1}{\overset{H_0}{\gtrless}} \tau \tag{18}$$

where τ is a threshold related to the probability of false alarm PFA and the probability of detection PD of the change detector.

Note that the structure of the manifold defined by the vector $\boldsymbol{v}_P$ is directly related to the image modalities that are under consideration. However, the manifold learning defined in Section III-B and the change detection strategy defined by (17) and (18) can be applied to any sequence of images and do not depend on the kind of sensors involved (optical, radar, etc.). In particular, the proposed change detection methodology can be used for homogeneous as well as for heterogeneous datasets, as shown in the next section.

IV. SIMULATION RESULTS

This section studies the relevance of the model introduced in Section II-C and the performance of the change detector defined in Section III-D to detect changes between synthetic and real images. The change detection results are compared with those obtained with different classical methods, namely, mean pixel difference, mean pixel ratio, correlation coefficient and mutual information. The first two reference change detection methods were provided by the ORFEO Toolbox [60]. The change detection results are compared with those obtained with classical methods and with the method of [43] based on conditional copulas. Note that the method presented in [43] is one of the more recent change detection methods that can be applied to both homogeneous and heterogeneous images.

A. Synthetic Images

The images shown in Fig. 12 were created by generating a synthetic scene P composed of triangular patches representing the different objects contained in the image, following the steps described in Section II-D. This synthetic scene was corrupted by additive Gaussian noise with SNR $= 30dB$ to form the optical image. To generate the SAR image, a known transformation was applied to the scene P which

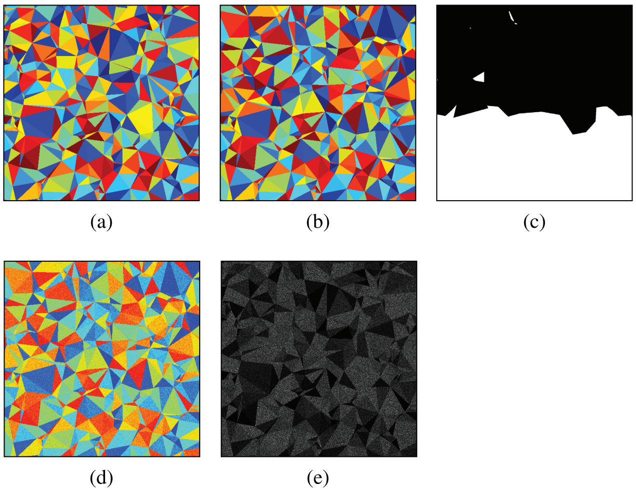

(a) (b) (c)

(d) (e)

Fig. 12. Example of synthetic images with changed and unchanged areas, with $T_{\mathrm{Opt}}(P) = P$ and $T_{\mathrm{SAR}}(P) = P(1-P)$. (a) P_{Opt}. (b) P_{SAR}. (c) Change mask. (d) I_{Opt}. (e) I_{SAR}.

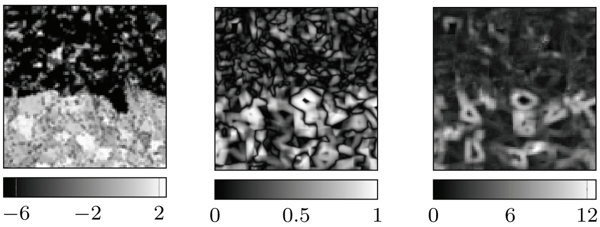

(a) (b) (c)

Fig. 13. Estimated change maps for the images of Fig. 12. Bright areas indicate high similarity, while dark areas indicate low similarity. (a) $\log(\delta_W)$. (b) Correlation Coeff. (c) Mutual Information.

was corrupted by multiplicative gamma noise (with shape parameter equal to $L = 5$). More precisely, the following transformation

$$\boldsymbol{v}_P = \left[T_{\mathrm{Opt}}(P), T_{\mathrm{SAR}}(P)\right] \tag{19}$$

with $T_{\mathrm{SAR}}(P) = T_{\mathrm{Opt}}(P)\left[1 - T_{\mathrm{Opt}}(P)\right]$ was used for experiments conducted on synthetic data.

The images displayed in Fig. 13 compare the proposed estimated change detection map with those obtained using the correlation coefficient, the mutual information, the mean pixel difference and the mean pixel ratio. These results were obtained using window sizes optimized by cross validation to produce the best performance for each method. More precisely, following Remark 2, we obtained window sizes of 20×20 pixels for the proposed method, 50×50 pixels for the correlation coefficient and the mutual information, and 21×21 pixels for the mean pixel difference and mean pixel ratio. Note that the difference in the window sizes is due to the inefficiency of the correlation coefficient and the mutual information for small homogeneous windows (as described in Section III-A and observed in Fig. 6), thus requiring bigger (and thus more likely heterogeneous) windows. The mutual information was computed by integrating numerically the joint distribution derived in Section II-C.

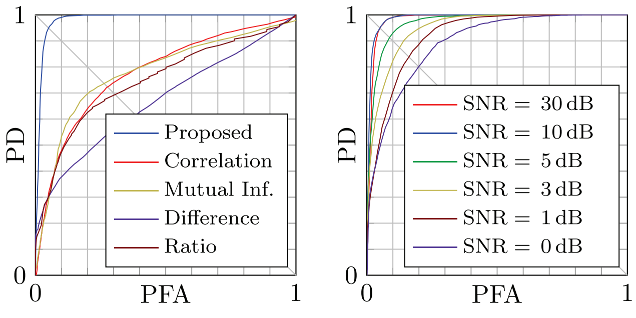

(a) (b)

Fig. 14. ROC curves for synthetic images (a) for different methods, (b) for the proposed method with different SNRs.

TABLE I
PERFORMANCE OF DIFFERENT CHANGE DETECTION METHODS FOR THE IMAGES OF FIG. 14(A)

Method	PFA = PND
Proposed method	4.41%
Correlation Coefficient	27.68%
Mutual Information	26.35%
Mean Pixel Difference	38.47%
Mean Pixel Ratio	30.60%

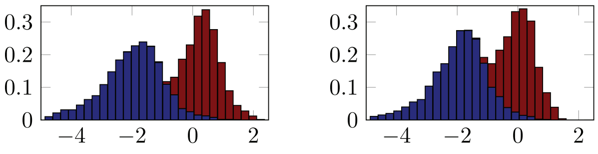

(a) (b)

Fig. 15. Histograms of the similarity measure $\log(\delta_W)$ for $\widehat{K}^* = \widehat{K}$ and $\widehat{K}^* = \widehat{K}+1$. The blue and red bins correspond to the changed and unchanged areas, respectively. (a) Histogram of $\log\left(\delta_W\right)$ for $\widehat{K}^* = \widehat{K}$ (no overestimation). (b) Histogram of $\log(\delta_W)$ for $\widehat{K}^* = \widehat{K}+1$.

Fig. 14(a) displays the ROC curves for the different methods. In order to compare the performance of the different methods, we propose to choose a detection threshold corresponding to PFA = 1 − PD = PND, located in the diagonal line displayed in Fig. 14(b). Table I shows the values of PFA obtained with the different methods, confirming the good performance of the proposed method.

We evaluated the performance of the proposed strategy for different values of the signal to noise ratio (SNR) associated with the optical image. ROC curves obtained for different SNRs are shown in Fig. 14(a), where it can be observed that the change detection performance is not affected for SNR $\geq$ 10dB. The performance drop obtained for lower SNR is mainly due to errors in the estimation of the mixture parameters (the parameters of the different mixture components are difficult to estimate in the presence of significant noise).

It is interesting to study the effect of overestimating the number of mixture components K on the detection performance. As discussed before, this will generally result in a high variance for the manifold samples $\widehat{\boldsymbol{v}}_{W,k}$ associated with small values of $\widehat{w}_k$. However, (17) shows that the terms associated with small values of $\widehat{w}_k$ have small impact on the final value of the test statistics δ_W, mitigating the overestimation effects. To analyze this behavior, we have conducted simulations by running the EM algorithm with an overestimated number of components $\widehat{K}^* = \widehat{K} + i$, for $i = 1, \ldots, 4$. The corresponding ROC curves are displayed in Fig. 16, where it can be observed that the detector is characterized by a small performance drop when the overestimation is not too important. This result is also illustrated in Fig. 15 showing that the distributions of δ_W are close for $\widehat{K}^* = \widehat{K}$ and $\widehat{K}^* = \widehat{K} + 1$ under both hypotheses (“change” and “no change”).

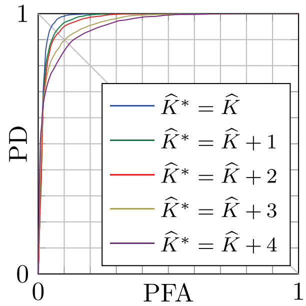

Fig. 16. Performance of the change detector for different values of $\widehat{K}^*$.

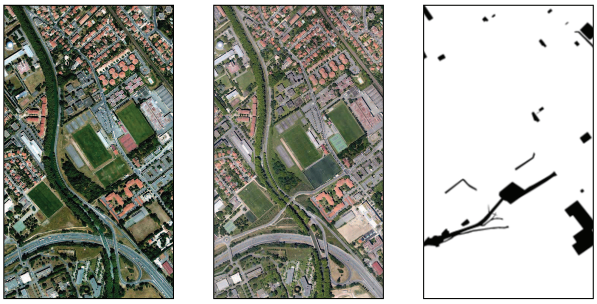

(a) I_{old} (b) I_{new} (c) Change mask

Fig. 17. Two optical images for the same area in the south of Toulouse at two time instants (a) and (b), and the corresponding change mask (c).

B. Pair of Real Optical Images

Fig. 17 shows two optical images corresponding to an area located in the south of Toulouse (France) acquired at two different time instants (December 31, 2006 and June 2, 2012) and the corresponding change mask. Both images were scaled and co-registered, resulting in a pixel resolution of 0.66m for both images. The change mask was provided by a photo interpreter. The observed changes between the two images are mainly due to the construction of a new road and some of new buildings. Note that even if the two sensors are optical sensors, they have different brightness, contrast and saturation.

Fig. 18 shows the detection maps obtained with the proposed method, the correlation coefficient, the mutual information, the conditional copulas[1] [43], the mean pixel

---

[1] The authors would like to thank Grégoire Mercier for providing the results obtained with the conditional copulas.

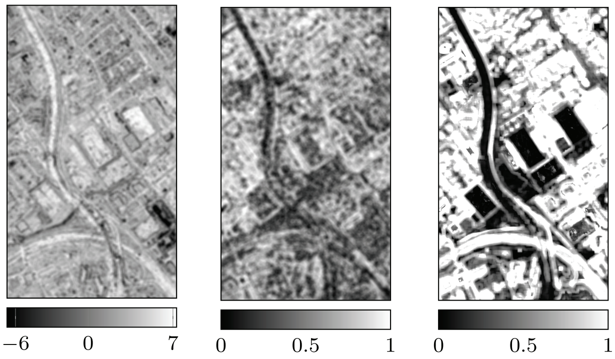

(a) log (δ_W) (b) Correlation (c) Copulas

Fig. 18. Detection maps obtained with the proposed method (a), correlation coefficient (b) and conditional copulas (c). Bright areas indicate high similarity, while dark areas indicate low similarity.

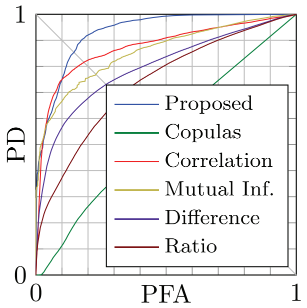

Fig. 19. ROC curves for the optical images of Fig. 17.

TABLE II
PERFORMANCE OF DIFFERENT CHANGE DETECTION
METHODS FOR THE IMAGES OF FIG. 19

Method	PFA = PND
Proposed method	14.60%
Conditional Copulas	46.45%
Correlation Coefficient	18.39%
Mutual Information	23.07%
Mean Pixel Difference	26.90%
Mean Pixel Ratio	31.87%

difference and the mean pixel ratio. These results were obtained with moving windows of 10 × 10 pixels for the proposed method, 20 × 20 for the correlation coefficient and the mutual information and 21 × 21 pixels for the remaining methods. Fig. 19 shows the corresponding ROCs computed using the ground truth of Fig. 17(c). Since the pixel intensities in the two optical images have linear dependencies, the correlation coefficient method performance is quite good, as expected. Since the dataset consists of two optical images the mean pixel difference is expected to outperform the mean pixel ratio (which is more adequate to detect changes on SAR images). However, an important performance loss can be observed in both pixel-wise approaches. Table II shows the probabilities of false alarm obtained with the different methods. Again, the proposed method outperforms existing techniques.

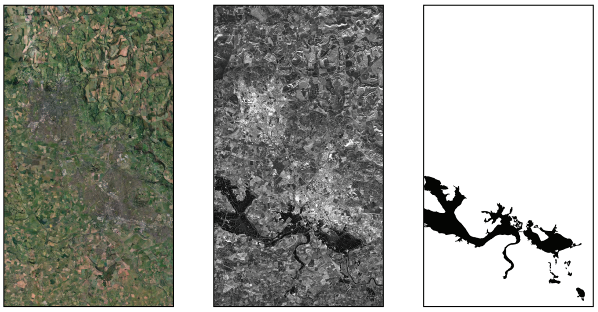

(a) I_{old} (b) I_{new} (c) Change mask

Fig. 20. Optical and SAR images associated with the same area in Gloucester before (a) and after (b) a flooding, and the corresponding change mask (c).

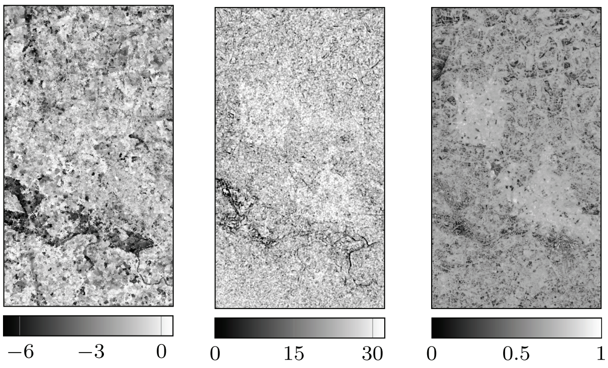

(a) log (δ_W) (b) Correlation (c) Copulas

Fig. 21. Change detection maps obtained with the proposed method (a), the correlation coefficient (b) and the conditional copulas (c). Bright areas indicate high similarity, while dark areas indicate low similarity.

TABLE III
PERFORMANCE OF DIFFERENT CHANGE DETECTION
METHODS FOR THE IMAGES OF FIG. 22

Method	PFA = PND
Proposed method	14.58%
Conditional Copulas	23.96%
Correlation Coefficient	31.19%
Mutual Information	23.12%
Mean Pixel Difference	21.75%
Mean Pixel Ratio	18.61%

C. Heterogeneous Optical and SAR Images

Fig. 20 shows an optical and a SAR image acquired before and during a flooding in Gloucester (UK) and the corresponding change mask. The SAR image was obtained by the TerraSAR-X satellite with HH polarization in 2007. Both images were scaled and co-registered, resulting in a pixel resolution of 7.27m for both images. The change mask was provided by a photo interpreter.

The sizes of the moving windows used for these experiments were 10 × 10 pixels for the proposed method, the correlation coefficient and the mutual information, 21 × 21 pixels for the mean pixel difference and the mean pixel ratio,

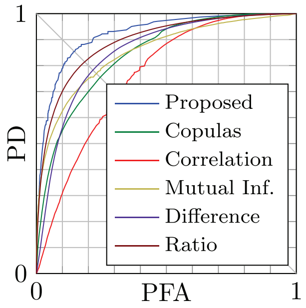

Fig. 22. ROCs for the heterogeneous images in Fig. 20.

and 9 × 9 pixels for the conditional copulas. Fig. 21 shows the change detection maps obtained for the different methods, while the corresponding probabilities of false alarm are reported in Table III. As expected, the mutual information performance remains unchanged while the correlation coefficient is heavily affected by the multimodality of the dataset. The particularly good performance of the mean pixel ratio method is a consequence of the particular nature of the changes present in this dataset, where water is captured by the radar sensor as an homogeneous dark surface.

V. CONCLUSION

The first part of this paper introduced a new statistical model to describe the distribution of any number of joint images independently of the kind of sensors used to obtain these images. The proposed model was based on a mixture of multi-dimensional distributions whose parameters can be estimated by the expectation-maximization algorithm. This mixture of distributions can be used to determine standard similarity measures such as the mutual information and is thus interesting for many potential applications. The second part of this article introduced a new change detection strategy based on a test statistics estimated from training images without changes. This strategy was compared to classical methods for synthetic and real data showing encouraging results. This paper mainly concentrated on the detection of changes between optical and synthetic aperture radar images. However, the proposed model could be interesting for many other applications such as image segmentation [61], [62], image registration [34], [63], database updating [64], image indexing or image classification. Moreover, when the dataset consists mostly of unchanged areas, the whole image can be used for the manifold estimation since the influence of the changed areas are negligible. In this case the proposed strategy can be used to build a completely unsupervised change detector. These applications would deserve to be studied in future work.

ACKNOWLEDGMENT

The authors are very grateful to Grégoire Mercier from ENST Bretagne for providing the simulations results related to the method proposed in [43] and for fruitful discussions about this paper.

REFERENCES

[1] C. D. Storie, J. Storie, and G. Salinas de Salmuni, “Urban boundary extraction using 2-component polarimetric SAR decomposition,” in *Proc. IEEE Int. Geosci. Remote Sens. Symp. (IGARSS)*, Munich, Germany, Jul. 2012, pp. 5741–5744.

[2] C. Tison, J.-M. Nicolas, F. Tupin, and H. Maitre, “A new statistical model for Markovian classification of urban areas in high-resolution SAR images,” *IEEE Trans. Geosci. Remote Sens.*, vol. 42, no. 10, pp. 2046–2057, Oct. 2004.

[3] V. Poulain, J. Inglada, M. Spigai, J.-Y. Tourneret, and P. Marthon, “High resolution optical and sar image fusion for road database updating,” in *Proc. IEEE Int. Geosci. Remote Sens. Symp. (IGARSS)*, Honolulu, HI, USA, Jul. 2010, pp. 2747–2750.

[4] R. A. Schowengerdt, *Remote Sensing: Models and Methods for Image Processing*. Amsterdam, The Netherlands: Elsevier, 2006.

[5] J. C. Curlander and R. N. McDonough, *Synthetic Aperture Radar: Systems and Signal Processing* (Remote Sensing and Image Processing). New York, NY, USA: Wiley, 1991.

[6] W. C. Carrara, R. S. Goodman, and R. M. Majewski, *Spotlight Synthetic Aperture Radar: Signal Processing Algorithms*. Norwood, MA, USA: Artech House, 1995.

[7] J. Inglada and G. Mercier, “A new statistical similarity measure for change detection in multitemporal SAR images and its extension to multiscale change analysis,” *IEEE Trans. Geosci. Remote Sens.*, vol. 45, no. 5, pp. 1432–1445, May 2009.

[8] P. Uprety and F. Yamazaki, “Use of high-resolution SAR intensity images for damage detection from the 2010 Haiti earthquake,” in *Proc. IEEE Int. Geosci. Remote Sens. Symp. (IGARSS)*, Munich, Germany, Jul. 2012, pp. 6829–6832.

[9] F. Bovolo and L. Bruzzone, “A theoretical framework for unsupervised change detection based on change vector analysis in the polar domain,” *IEEE Trans. Geosci. Remote Sens.*, vol. 45, no. 1, pp. 218–236, Jan. 2007.

[10] A. Singh, “Review article digital change detection techniques using remotely-sensed data,” *Int. J. Remote Sens.*, vol. 10, no. 6, pp. 989–1003, 1989.

[11] T. Fung, “An assessment of TM imagery for land-cover change detection,” *IEEE Trans. Geosci. Remote Sens.*, vol. 28, no. 4, pp. 681–684, Jul. 1990.

[12] L. Bruzzone and D. F. Prieto, “Automatic analysis of the difference image for unsupervised change detection,” *IEEE Trans. Geosci. Remote Sens.*, vol. 38, no. 3, pp. 1171–1182, May 2000.

[13] L. Bruzzone and D. F. Prieto, “An adaptive semiparametric and context-based approach to unsupervised change detection in multitemporal remote-sensing images,” *IEEE Trans. Image Process.*, vol. 11, no. 4, pp. 452–466, Apr. 2002.

[14] T. Celik, “Unsupervised change detection in satellite images using principal component analysis and k-means clustering,” *IEEE Geosci. Remote Sens. Lett.*, vol. 6, no. 4, pp. 772–776, Oct. 2009.

[15] L. Bruzzone and D. Fernández Prieto, “An adaptive parcel-based technique for unsupervised change detection,” *Int. J. Remote Sens.*, vol. 21, no. 4, pp. 817–822, 2000.

[16] G. Pajares, J. J. Ruz, and J. M. de la Cruz, “Performance analysis of homomorphic systems for image change detection,” in *Pattern Recognition and Image Analysis* (Lecture Notes in Computer Science), vol. 3522, J. S. Marques, N. Pérez de la Blanca, and P. Pina, Eds. Berlin, Germany: Springer-Verlag, 2005, pp. 563–570.

[17] T. Celik, “Multiscale change detection in multitemporal satellite images,” *IEEE Geosci. Remote Sens. Lett.*, vol. 6, no. 4, pp. 820–824, Oct. 2009.

[18] T. Celik and M. Kai-Kuang, “Unsupervised change detection for satellite images using dual-tree complex wavelet transform,” *IEEE Trans. Geosci. Remote Sens.*, vol. 48, no. 3, pp. 1199–1210, Mar. 2010.

[19] S. Ghosh, L. Bruzzone, S. Patra, F. Bovolo, and A. Ghosh, “A context-sensitive technique for unsupervised change detection based on Hopfield-type neural networks,” *IEEE Trans. Geosci. Remote Sens.*, vol. 45, no. 3, pp. 778–789, Mar. 2007.

[20] A. Ghosh, B. N. Subudhi, and L. Bruzzone, “Integration of Gibbs Markov random field and Hopfield-type neural networks for unsupervised change detection in remotely sensed multitemporal images,” *IEEE Trans. Image Process.*, vol. 22, no. 8, pp. 3087–3096, Aug. 2013.

[21] F. Pacifici, F. Del Frate, C. Solimini, and W. J. Emery, “An innovative neural-net method to detect temporal changes in high-resolution optical satellite imagery,” *IEEE Trans. Geosci. Remote Sens.*, vol. 45, no. 9, pp. 2940–2952, Sep. 2007.

[22] G. Pajares, “A Hopfield neural network for image change detection,” *IEEE Trans. Neural Netw.*, vol. 17, no. 5, pp. 1250–1264, Sep. 2006.

[23] F. Pacifici and F. Del Frate, “Automatic change detection in very high resolution images with pulse-coupled neural networks,” *IEEE Geosci. Remote Sens. Lett.*, vol. 7, no. 1, pp. 58–62, Jan. 2010.

[24] H. Nemmour and Y. Chibani, “Multiple support vector machines for land cover change detection: An application for mapping urban extensions,” *ISPRS J. Photogrammetry Remote Sens.*, vol. 61, no. 2, pp. 125–133, 2006.

[25] R. J. Radke, S. Andra, O. Al-Kofahi, and B. Roysam, “Image change detection algorithms: A systematic survey,” *IEEE Trans. Image Process.*, vol. 14, no. 3, pp. 294–307, Mar. 2005.

[26] R. Touzi, A. Lopés, and P. Bousquet, “A statistical and geometrical edge detector for SAR images,” *IEEE Trans. Geosci. Remote Sens.*, vol. 26, no. 6, pp. 764–773, Nov. 1988.

[27] E. J. M. Rignot and J. J. van Zyl, “Change detection techniques for ERS-1 SAR data,” *IEEE Trans. Geosci. Remote Sens.*, vol. 31, no. 4, pp. 896–906, Jul. 1993.

[28] J. D. Villasenor, D. R. Fatland, and L. D. Hinzman, “Change detection on Alaska’s north slope using repeat-pass ERS-1 SAR images,” *IEEE Trans. Geosci. Remote Sens.*, vol. 31, no. 1, pp. 227–236, Jan. 1993.

[29] R. Fjortoft, A. Lopés, P. Marthon, and E. Cubero-Castan, “An optimal multiedge detector for SAR image segmentation,” *IEEE Trans. Geosci. Remote Sens.*, vol. 36, no. 3, pp. 793–802, May 1998.

[30] Y. Bazi, L. Bruzzone, and F. Melgani, “An unsupervised approach based on the generalized Gaussian model to automatic change detection in multitemporal SAR images,” *IEEE Trans. Geosci. Remote Sens.*, vol. 43, no. 4, pp. 874–887, Apr. 2005.

[31] C. Carincotte, S. Derrode, and S. Bourennane, “Unsupervised change detection on SAR images using fuzzy hidden Markov chains,” *IEEE Trans. Geosci. Remote Sens.*, vol. 44, no. 2, pp. 432–441, Feb. 2006.

[32] L. Bruzzone and S. B. Serpico, “An iterative technique for the detection of land-cover transitions in multitemporal remote-sensing images,” *IEEE Trans. Geosci. Remote Sens.*, vol. 35, no. 4, pp. 858–867, Jul. 1997.

[33] C. Pratola, F. Del Frate, G. Schiavon, and D. Solimini, “Toward fully automatic detection of changes in suburban areas from VHR SAR images by combining multiple neural-network models,” *IEEE Trans. Geosci. Remote Sens.*, vol. 51, no. 4, pp. 2055–2066, Apr. 2013.

[34] F. Chatelain, J.-Y. Tourneret, J. Inglada, and A. Ferrari, “Bivariate gamma distributions for image registration and change detection,” *IEEE Trans. Image Process.*, vol. 16, no. 7, pp. 1796–1806, Jul. 2007.

[35] G. Quin, B. Pinel-Puyssegur, J.-M. Nicolas, and P. Loreaux, “MIMOSA: An automatic change detection method for SAR time series,” *IEEE Trans. Geosci. Remote Sens.*, vol. 52, no. 9, pp. 5349–5363, Sep. 2014.

[36] L. Giustarini, R. Hostache, P. Matgen, G. J.-P. Schumann, P. D. Bates, and D. C. Mason, “A change detection approach to flood mapping in urban areas using TerraSAR-X,” *IEEE Trans. Geosci. Remote Sens.*, vol. 51, no. 4, pp. 2417–2430, Apr. 2013.

[37] J. Inglada and A. Giros, “On the possibility of automatic multisensor image registration,” *IEEE Trans. Geosci. Remote Sens.*, vol. 42, no. 10, pp. 2104–2120, Oct. 2004.

[38] J. Inglada, “Similarity measures for multisensor remote sensing images,” in *Proc. IEEE Int. Geosci. Remote Sens. Symp. (IGARSS)*, vol. 1. Toronto, ON, Canada, Jun. 2002, pp. 104–106.

[39] H.-M. Chen, P. K. Varshney, and M. K. Arora, “Performance of mutual information similarity measure for registration of multitemporal remote sensing images,” *IEEE Trans. Geosci. Remote Sens.*, vol. 41, no. 11, pp. 2445–2454, Nov. 2003.

[40] N. Kwak and C.-H. Choi, “Input feature selection by mutual information based on Parzen window,” *IEEE Trans. Pattern Anal. Mach. Intell.*, vol. 24, no. 12, pp. 1667–1671, Dec. 2002.

[41] A. M. Fraser and H. L. Swinney, “Independent coordinates for strange attractors from mutual information,” *Phys. Rev. A*, vol. 33, pp. 1134–1140, Feb. 1986.

[42] M. Chabert and J.-Y. Tourneret, “Bivariate Pearson distributions for remote sensing images,” in *Proc. IEEE Int. Geosci. Remote Sens. Symp. (IGARSS)*, Vancouver, BC, Canada, Jul. 2011, pp. 4038–4041.

[43] G. Mercier, G. Moser, and S. B. Serpico, “Conditional copulas for change detection in heterogeneous remote sensing images,” *IEEE Trans. Geosci. Remote Sens.*, vol. 46, no. 5, pp. 1428–1441, May 2008.

[44] C. Oliver and S. Quegan, *Understanding Synthetic Aperture Radar Images*. Boston, MA, USA: Artech House, 1998.

[45] V. S. Frost, J. A. Stiles, K. S. Shanmugan, and J. Holtzman, “A model for radar images and its application to adaptive digital filtering of multiplicative noise,” *IEEE Trans. Pattern Anal. Mach. Intell.*, vol. PAMI-4, no. 2, pp. 157–166, Mar. 1982.

[46] J.-S. Lee, “Speckle suppression and analysis for synthetic aperture radar images,” *Opt. Eng.*, vol. 25, no. 5, p. 255636, May 1986.

[47] K. R. Castleman, *Digital Image Processing*. Englewood Cliffs, NJ, USA: Prentice-Hall, 1996.

[48] L. Liu, Y. Jiang, and C. Wang, “Noise analysis and image restoration for optical sparse aperture systems,” in *Proc. Int. Workshop Edu. Technol. Training, Geosci. Remote Sens.*, vol. 1. Shanghai, China, Dec. 2008, pp. 353–356.

[49] A. P. Dempster, N. M. Laird, and D. B. Rubin, “Maximum likelihood from incomplete data via the EM algorithm,” *J. Roy. Statist. Soc., B*, vol. 39, no. 1, pp. 1–38, 1977.

[50] G. Celeux and J. Diebolt, “The SEM algorithm: A probabilistic teacher algorithm derived from the EM algorithm for the mixture problem,” *Comput. Statist. Quart.*, vol. 2, no. 1, pp. 73–82, 1985.

[51] D. T. Lee and B. J. Schachter, “Two algorithms for constructing a Delaunay triangulation,” *Int. J. Comput. Inf. Sci.*, vol. 9, no. 3, pp. 219–242, 1980.

[52] S. Kotz, N. Balakrishnan, and N. L. Johnson, *Continuous Multivariate Distributions, Models and Applications*. New York, NY, USA: Wiley, 2004.

[53] G. McLachlan and D. Peel, *Finite Mixture Models*. New York, NY, USA: Wiley, 2004.

[54] O. Schwander, A. J. Schutz, F. Nielsen, and Y. Berthoumieu, “k-MLE for mixtures of generalized Gaussians,” in *Proc. IEEE 21st Int. Conf. Pattern Recognit.*, Tsukuba, Japan, Nov. 2012, pp. 2825–2828.

[55] E. L. Lehmann and G. Casella, *Theory of Point Estimation* (Springer Texts in Statistics). New York, NY, USA: Springer-Verlag, 1998.

[56] M. A. T. Figueiredo and A. K. Jain, “Unsupervised learning of finite mixture models,” *IEEE Trans. Pattern Anal. Mach. Intell.*, vol. 24, no. 3, pp. 381–396, Mar. 2002.

[57] L. Wojnar, *Image Analysis: Applications in Materials Engineering*. New York, NY, USA: Taylor & Francis, 1998.

[58] J. A. Peacock, “Two-dimensional goodness-of-fit testing in astronomy,” *Monthly Notices Roy. Astronomical Soc.*, vol. 202, pp. 615–627, Feb. 1983.

[59] W. W. Peterson, T. Birdsall, and W. Fox, “The theory of signal detectability,” *Trans. IRE Prof. Group Inf. Theory*, vol. 4, no. 4, pp. 171–212, Sep. 1954.

[60] OTB Development Team. (2014). *The ORFEO Toolbox Software Guide*. [Online]. Available: http://orfeo-toolbox.org/

[61] C. Carson, S. Belongie, H. Greenspan, and J. Malik, “Blobworld: Image segmentation using expectation-maximization and its application to image querying,” *IEEE Trans. Pattern Anal. Mach. Intell.*, vol. 24, no. 8, pp. 1026–1038, Aug. 2002.

[62] M. S. Allili, D. Ziou, N. Bouguila, and S. Boutemedjet, “Image and video segmentation by combining unsupervised generalized Gaussian mixture modeling and feature selection,” *IEEE Trans. Circuits Syst. Video Technol.*, vol. 20, no. 10, pp. 1373–1377, Oct. 2010.

[63] F. Maes, A. Collignon, D. Vandermeulen, G. Marchal, and P. Suetens, “Multimodality image registration by maximization of mutual information,” *IEEE Trans. Med. Imag.*, vol. 16, no. 2, pp. 187–198, Apr. 1997.

[64] M. Chabert, J. Y. Tourneret, V. Poulain, and J. Inglada, “Logistic regression for detecting changes between databases and remote sensing images,” in *Proc. IEEE Int. Geosci. Remote Sens. Symp. (IGARSS)*, Honolulu, HI, USA, Jul. 2010, pp. 3198–3201.

Jorge Prendes was born in Santa Fe, Argentina, in 1987. He received the Engineering (Hons.) degree in electrical engineering from the Buenos Aires Institute of Technology (ITBA), Buenos Aires, Argentina, in 2010. He was a Research Engineer in Signal Processing with the Applied Digital Electronics Group, ITBA, until 2012.

He is currently pursuing the Ph.D. degree in signal processing with the Supélec, TéSA Laboratory, Toulouse, France, and the Signal and Communication Group, Institut de Recherche en Informatique de Toulouse, Toulouse. His main research interests include image processing, applied mathematics, and pattern recognition.

Marie Chabert received the Engineering degree in electronics and signal processing from the École Normale Supérieure d’Electronique, d’Electrotechnique, d’Informatique, d’Hydraulique et des Télécommunications de Toulouse (ENSEEIHT), Toulouse, France, in 1994, and the M.Sc. degree in signal processing, the Ph.D. degree in signal processing, and the H.D.R. degree from the National Polytechnic Institute of Toulouse (INPT), Toulouse, in 1994, 1997, and 2007, respectively.

She is currently an Associate Professor of Signal and Image Processing. She is with the Engineering School INPT-ENSEEIHT, University of Toulouse, Toulouse. She is conducting her research with the Signal and Communication Team, Institut de Recherche en Informatique de Toulouse (UMR 5505 of the CNRS), Toulouse. Her research interests include nonuniform sampling, time-frequency diagnosis and condition monitoring, and statistical modeling of heterogeneous data in remote sensing.

Frédéric Pascal received the master’s (Hons.) degree in applied statistics from University Paris VII-Jussieu, Paris, France, in 2003, with a focus on probabilities, statistics and applications for signal, image and networks, and the Ph.D. degree in signal processing from University Paris X-Nanterre, Nanterre, France, in 2006, by Pr. Philippe Forster with a focus on detection and estimation in compound gaussian noise. His Ph.D. thesis was in collaboration with the French Aerospace Laboratory, Palaiseau, France. From 2006 to 2008, he held a post-doctoral position with the Signal Processing and Information Team, Système et Applications des Technologies de l’Information et de l’Energie Laboratory, CNRS, École Normale Supérieure, Cachan, France. From 2008 to 2011 and 2012 to 2013, he was an Assistant Professor and Associate Professor with SONDRA, the French-Singaporean Laboratory of Supélec, Gif-sur-Yvette, France. He received the Research Directorship Habilitation thesis in Signal Processing from the University of Paris-Sud, Orsay, France, in 2012. Since 2014, he has been a Full Professor with the SONDRA Laboratory, Supélec. His research interests contain estimation, detection, and classification in statistical signal processing and radar processing.

Alain Giros received the Physics Engineering degree from the École Normale Supérieure de Physique de Marseille, Marseille, France, in 1982, with a specialization in optics and image processing.

He has been with the Centre National d’ Études Spatiales (CNES), Toulouse, France. He began his carrier with the SPOT 1 Project Team, where he was responsible for the whole image processing software. Then, he was responsible for the development of several image processing systems, including DALI (the worldwide catalog of SPOT images), several image quality assessment systems for SPOT, and the vegetation user services facility. He has been interested in automated image registration since the mid-1990s and promoting this research subject at CNES

He is currently in charge of the development of image processing techniques mainly in the field of image time series processing, automated registration, and image information mining.

Jean-Yves Tourneret received the Engineering degree in electrical engineering from the École Normale Supérieure d’Electronique, d’Electrotechnique, d’Informatique, d’Hydraulique et des Télécommunications de Toulouse, Toulouse, France, in 1989, and the Ph.D. degree from the National Polytechnic Institute of Toulouse, Toulouse, in 1992. He is currently a Professor with the University of Toulouse, Toulouse, and a member of the Institut de Recherche en Informatique de Toulouse Laboratory (UMR 5505 of the CNRS). His research activities are centered on statistical signal and image processing with a particular interest to Bayesian and Markov chain Monte Carlo methods.

He was involved in the organization of several conferences, including the 2002 European Conference on Signal Processing (Program Chair), the 2006 International Conference on Acoustics, Speech, and Signal Processing (plenaries), the 2012 Statistical Signal Processing Workshop (SSP) (international liaisons), the 2013 International Workshop on Computational Advances in Multi-Sensor Adaptive Processing (CAMSAP) (local arrangements), the 2014 SSP (special sessions), and the 2014 Workshop on Machine Learning for Signal Processing (special sessions). He was the General Chair of the CIMI Workshop on Optimization and Statistics in Image Processing in Toulouse in 2013 (with F. Malgouyres and D. Kouamé). He will be the General Chair of CAMSAP in 2015 (with P. Djuric). He has been a member of different technical committees, including the Signal Processing Theory and Methods Committee of the IEEE Signal Processing Society (2001–2007, 2010-present). He was an Associate Editor of the IEEE Transactions on Signal Processing (2008–2011) and has served as an Associate Editor of the *EURASIP Journal on Signal Processing* since 2013.